



Activation of oxalic acid via dual-pathway over single-atom Fe catalysts: Mechanism and membrane application

Xiaoke Zhang^{a,1}, Jianhui Liu^{b,1}, Xiucheng Zheng^{b,*}, Rong Chen^{a,c}, Meng Zhang^{b,*}, Zhongyi Liu^b, Zhiyuan Wang^a, Jun Li^{a,b,**}

^a Henan Institute of Advanced Technology, Zhengzhou University, Zhengzhou 450052, PR China

^b College of Chemistry, Zhengzhou University, Zhengzhou 450001, PR China

^c School of Chemistry and Environmental Engineering, Wuhan Institute of Technology, Wuhan 430205, PR China

ARTICLE INFO

Keywords:

Oxalic acid activation
Fe single atom
Carbon dioxide free radical
Cr(VI) removal
Photocatalysis

ABSTRACT

Oxalic acid (OA), together with its ligand, appears in diverse biotic and abiotic processes in nature. However, the applications of the photochemical property of OA and its complexes in environmental purification are scarce. Herein, we reported a Fe single-atom catalyst with Fe-N₄ configuration supported on g-C₃N₄ (Fe-CN) to activate OA for ultrahigh-efficiency removal of Cr(VI) under visible light irradiation through dual pathways: the photodissociation of [Fe^{III}(C₂O₄)]⁺ and the reaction between OA and photogenerated holes, achieving the generation of •CO₂. The introduction of Fe-N₄ favors the formation of configuration [Fe^{III}(C₂O₄)]⁺ and fabricates the electron transfer channel from catalyst to OA, further decreases the energy barriers of •CO₂ generation, and thereafter efficiently facilitates the C-C cleavage for the generate of •CO₂. Meanwhile, the strong coordination interaction over Fe single atoms and N atoms could enhance the separation efficiency of photo-carriers and further promote the reduction activity. Under optimal conditions, Fe-CN showed a 5.1-fold increase in photocatalytic kinetics contrast to pristine CN. The Fe-CN catalyst attached on fibrous membrane for treatment of flowing Cr(VI) wastewater exhibits 90% reduction efficiency over 10 h, which is expected to facilitate the practical application of the catalyst. The mechanism of OA activation with dual-pathway was unveiled by in-situ Fourier transform infrared spectra and theoretical calculations. This work provides an important guidance for the application of OA and its complexes to achieve the attenuation of toxic and harmful heavy metal in water restoration.

1. Introduction

Heavy metal contaminations pose significant threats to human health and ecological security, especially for hexavalent chromium (Cr(VI)) with high toxicity and biologically incompatible property [1]. Even low concentration of Cr(VI) (> 50 µg/L) can pose a human health threat. Hence, the conversion of high-risk Cr(VI) to low-toxicity trivalent chromium (Cr(III)) is considerably crucial for ecological remediation [2]. The traditional methods of Cr(VI) reduction, for instance electrical plasma [3], bioremediation [4], electrocatalysis [5] and landfill after solidification, have been impeded by the problems of high energy consumption, high operating costs and low efficiency. In recent, researchers found that the addition of activators, such as H₂O₂ [6], ferrihydrite [7]

and sulfite [8], accelerated the reduction of Cr(VI). Developing high-efficiency, low-cost and eco-friendly activators is still a challenging and promising frontier.

Oxalic acid (OA), a natural and eco-friendly activator, is formed and consumed in plenty of biotic and abiotic processes. With strong coordination ability, OA can readily adsorbed on the surface of metal-based photocatalysts and formed metal-organic complexes, which could facilitate the activation via a ligand-to-metal charge transfer and promote the reductive reactions. The metal-OA complexes could produce active species under light irradiation such as carbon dioxide free radical (•CO₂), superoxide radical (•O₂) and hydroxyl radical (•OH) [9]. Among them, •CO₂ possesses strong reducibility (E₀ = −1.8 V vs. NHE), which account for the significant promotion in Cr(VI) reduction

* Corresponding authors.

** Corresponding author at: Henan Institute of Advanced Technology, Zhengzhou University, Zhengzhou 450052, PR China.

E-mail addresses: zhxch@zzu.edu.cn (X. Zheng), zhangmeng1991@zzu.edu.cn (M. Zhang), junli2019@zzu.edu.cn (J. Li).

¹ These authors contributed equally to this work.

efficiency. Fe-based catalyst has been confirmed to be an efficient activator for OA photochemical conversion in the field of environmental catalysis. To date, multiple kind of Fe-based photocatalysts have been investigated for OA activation, such as Fe⁰ [10], Fe₃O₄ [11], FeWO₄ [12] and so on, which showed superior catalytic performance. With the deepening of research, the photochemical properties and reaction mechanism of Fe-OA complexes are gradually unveiled. Interaction with different structures between OA and Fe-based system has been explored. Inner-sphere complexes were proposed in previous studies including mononuclear bidentate/monodentate (MB/MM, OA bonded with a single Fe atom via two/one O atoms) and binuclear bidentate (BB). Furthermore, MB structure has been confirmed to be the highest photochemical activity among them. However, most previous studies were focused on the metal-OA complexes structures. The investigation on the combination of the complexes structure and practical environment application is still lacking.

Single-atom catalysts (SACs) have attracted increasing attention due to their high metal atom utilization efficiency, unique electron structure and uniformly active center. An appropriate support for single-atom is vital, which can provide favorable anchoring sites to ensure high dispersion and stability [13]. Among many supporting materials, like metal-organic framework (MOF), zeolites and clays, graphitic carbon nitride (g-C₃N₄) stands out owing to its metal-free, stable, environmentally friendly, large specific surface area and easy fabrication properties. G-C₃N₄ could serve as an efficient support to stabilize the single metal atoms to form M-N_x structure via strong coordination interaction, which efficiently isolated metal single-atom to avoid aggregation of metal cluster and ion leaching [14]. Though the photocatalytic property of g-C₃N₄ is usually restricted by the high recombination of photogenerated charge, doping metal atoms is also a feasible strategy to enhance the optical and electrical properties of catalysts and the separation efficiency of photogenerated carriers. Duan et al. [15] utilized Fe single atom anchored on g-C₃N₄ (SAFe-CN) activate PMS for o-phenylphenol degradation. Isolated Fe atoms could enhance electron transfer, change electron distribution, and provide active sites for PMS activation, resulting in highly efficient utilization of PMS and excellent removal of pollutants [16]. However, the single-atom catalysts to OA activation for Cr(VI) reduction is rarely studied.

Herein, a series content of single Fe atoms were anchored on g-C₃N₄ support (Fe-CN) to activate OA for high-toxicity Cr(VI) reduction. The existence form of Fe single atom has been unveiled by aberration-corrected high-angle annular dark-field scanning transmission electron microscopy (AC-HAAD-STEM) and X-ray absorption fine structure (XAFS) measurement. Meanwhile, the photocatalytic performance of Fe-CN to OA activation was evaluated. The 0.4% Fe-CN-OA-vis system exhibited 100% reduction performance for Cr(VI) within 15 min. The mechanism of efficient Cr(VI) reduction by Fe-CN activated OA has been systematically discussed. The main mechanism of the generation of main active radical (•CO₂) with dual-pathway was confirmed by in-situ diffuse reflectance infrared Fourier (DRIFT) spectra and theoretical calculation. This work provides unique insights into the OA activation, which led to a guidance for heavy metal Cr(VI) reduction.

2. Experimental procedures

2.1. Synthesis of catalysts

The sources of reagents can be found in Text S1 of the supporting information. Typically, 4.0 g urea and a certain percentage of ferric nitrate were added into 15 mL deionized water with continuously stirring for 10 min. Afterwards, the mixture was dried and ground to obtain an orange homogeneous powder. The powder was calcined at 550 °C for 2 h in N₂ atmosphere to obtain the final product of x% Fe-CN (x%, the weight ratio of Fe(NO₃)₃ to urea: x = 0.2, 0.4 and 0.6). Pristine CN was prepared with calcination of urea under identical conditions.

2.2. Characterization

The crystal phases and chemical structures of the series of catalysts were identified by X-ray diffractometer (XRD, Panalytical XPert Pro) and Fourier transform infrared (FTIR, Thermo Scientific Nicolet 380) spectroscopy. The specific surface areas were measured by Micromeritics ASAP 2420-4MP applying the Brunauer-Emmett-Teller (BET) equation and Barrett-Johnal-Halenda (BJH) method. The morphology and microstructure of samples were characterized by scanning electron microscope (SEM, HITACHI SU8010), transmission electron microscope (TEM, JEOL JEM 2100 F) and AC-HAAD-STEM (FEI Theims Z). The surface chemical elements and bond characteristics were analyzed by X-ray photoelectron spectroscopy (XPS, Thermo Scientific Escalab Xi). The band gap width was reckoned by UV-vis diffuse reflectance (DRS, Japan Shimadzu UV-3600 spectrophotometer) spectra results. Radical identified by Electron spin resonance (ESR, Bruker EMX-PLUS) spectra. ⁵⁷Fe Mössbauer spectrum was collected using a Germany Wissel MS-500 spectrometer. The electrochemical performance of samples was measured on CHI 760E workstation, using silver/silver chloride electrode (Ag/AgCl) and Pt ring electrode as reference and counter electrode within 0.5 M Na₂SO₄ solution.

2.3. Catalytic procedure

Specifically, the catalyst (10 mg) was dispersed in the glass beaker with 100 mL Cr(VI) solution (5 mg/L) under 400 rpm rotary by magnetic stirring. Stirring for 15 min in the dark. Thereafter, a certain amount of OA was added to the mixture, and the reaction was initiated by visible irradiation (Xenon lamp, PLS SXE300, λ > 420 nm) at 25 °C. During the reaction, samples were taken every 5 min and analyzed by the colorimetric method of diphenylcarbazide. The pH of Cr(VI) solution was controlled through adding 0.1 M HNO₃ or 0.1 M NaOH. In radical trapping experiments, the methyl viologen dichloride (MVD, 2 mM), AgNO₃ (2 mM) or isopropanol (IPA, 100 mM) was added to scavenge •CO₂, e⁻ and •OH, respectively. All processes were performed in triplicate.

2.4. Calculation and measurement details

The details of XAFS measurement and calculation methods can be found in supporting information respectively (Text S2-S3).

2.5. Analysis

The apparent rate constants (*k*, min⁻¹) of Cr(VI) reduction were fitted by the first-order model according to Eq. 1:

$$\ln(C_t / C_0) = -k t \quad (1)$$

where *C_t* and *C₀* represent the concentration of Cr(VI) at a certain time (*t*) and initially, respectively.

The normalized per-surface area *k* (*k_{surface}*, g m⁻² min⁻¹) can be calculated as the Eq. 2:

$$k_{surface} = k / S \quad (2)$$

where *k* (min⁻¹) represents the rate constant obtained by Eq. 1, and *S* (m² g⁻¹) represents the surface area obtained by N₂ adsorption-desorption isotherm.

The flux of membranes *J* (L m⁻² h⁻¹) was computed as the Eq. 3:

$$J = V / (s \times t) \quad (3)$$

Where *V* (L) represents the volume of the flow solution in a certain time (*t*, h), *s* (m²) represents the effective filtration area of the membranes.

The average retention time (*T*) of Cr(VI) solution in the catalytic layer can be reckoned as Eq. 4:

$$T = V_{\text{pore}} / Q = (V_{\text{active}} \times \varepsilon) / Q = (A_{\text{active}} \times h_{\text{active}} \times \varepsilon) / Q = h_{\text{active}} / J(4)$$

Where V_{pore} represents the pore volume in the catalytic layer, and V_{active} , ε , h_{active} represent the volume, porosity, projected area, thickness of the catalyst coating layer, respectively. Q represents the feed Cr(VI) solution flux. To facilitate the calculation, we hypothesize the porosity as maximal as 100%.

3. Results and discussion

3.1. Synthesis and characterization of Fe single-atom catalysts

The Fe-CN catalyst was synthesized via pyrolysis of urea under N_2 atmosphere (Fig. S1). XRD patterns (Fig. S2) showed the characteristic peaks at 13.0° and 27.2° in the pristine CN, which corresponded to the (100) and (002) planes, respectively [17]. The almost unchanged diffraction feature of as-prepared samples (Fe-CN) was witnessed in comparison to CN. As the Fe content increased, the peak intensity of (100) and (002) planes was gradually weakened, indicating the reduction of condensation degree and distortion of in-plane structural units due to the presence of anchored Fe atoms. Besides, Fe-CN samples

exhibited similar stretching vibration bands with CN, which manifested the stability of CN matrix (Fig. S3). Typically, the absorption peak at 810 cm^{-1} was ascribed to the stretching vibration of s-triazine units. The featured peaks at $1200\text{--}1650$ and 3205 cm^{-1} corresponded to out-of-plane tri-s-triazine ring and the N-H bond stretching vibration, respectively [14]. No characteristic peak associated with Fe or Fe-based compounds was observed in the series of Fe-CN catalysts [16].

Electron microscopy images were performed to observe microstructure of as-prepared materials. As shown in Fig. S4, CN and 0.4% Fe-CN both exhibited wrinkled nanoflakes with numerous pores in SEM images. The TEM image (Fig. S5a) displayed that 0.4% Fe-CN had typical layer morphology ascribed to that of CN, while no Fe nanoparticle could be witnessed in HRTEM image (Fig. S5b), in agreement with the XRD and FT-IR results. The N_2 adsorption-desorption isotherm displayed the mesoporous feature of 0.4% Fe-CN, which possessed a higher specific surface area ($122.1\text{ m}^2\text{ g}^{-1}$), compared with CN ($58.2\text{ m}^2\text{ g}^{-1}$) (Fig. S6 and Table S1), indicating sufficient active sites were offered to enhance photocatalytic performance. The HAAD-STEM images illustrated the laminar properties of CN (Fig. 1a) and isolated Fe atoms which were

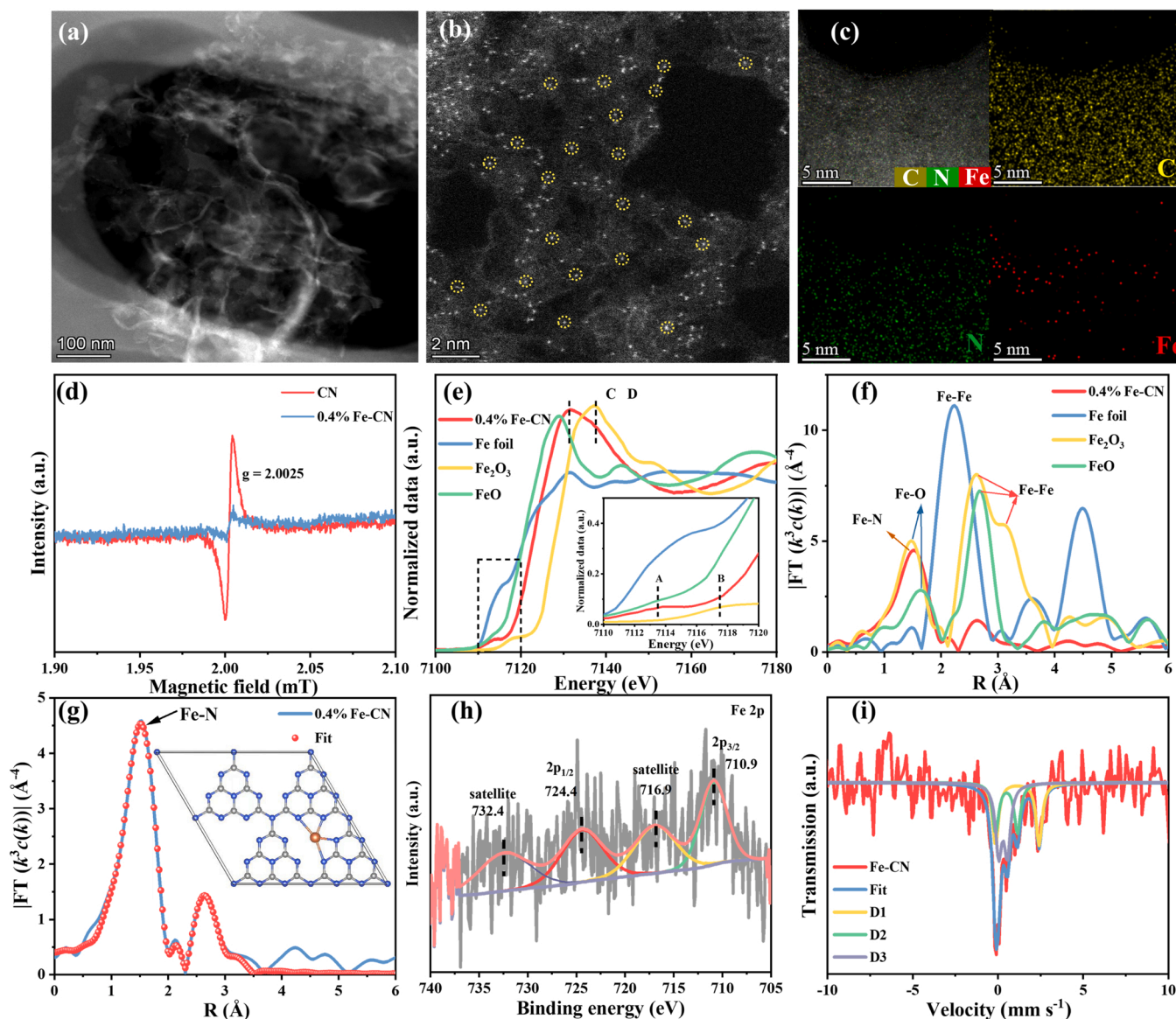


Fig. 1. (a–b) HAADF-STEM images and (c) elemental mapping images of 0.4% Fe-CN. (d) EPR spectra of CN and 0.4% Fe-CN. (e) Normalized Fe K-edge XANES spectra and (f) k^3 -weighted Fourier transform spectra of Fe foil, FeO, Fe_2O_3 and 0.4% Fe-CN. (g) EXAFS fitting curve in R space with the structural model of Fe-CN, Fe: brown, C: grey, N: blue. (h) XPS spectra of 0.4% Fe-CN: Fe 2p. (i) ^{57}Fe Mössbauer spectrum of 0.4% Fe-CN.

identified as bright dots in Fig. 1b. Meanwhile, element mapping results (Fig. 1c) verified the presence of C, N and Fe elements in 0.4% Fe-CN, and the uniform distribution of Fe atoms in the zone of CN support. The EPR signal peak intensity of Lorentz line at $g = 2.0025$ was significantly weakened after the introduction of Fe atoms, indicating the decrease of unpaired electrons and N defects in 0.4% Fe-CN, which was attributed to the coordination of Fe-N_x, resulting in improved photo-generated carriers separation and photocatalytic activity (Fig. 1d) [18, 19].

X-ray absorption near edge structure (XANES) spectra and extended X-ray absorption fine structure (EXAFS) spectra of 0.4% Fe-CN were recorded to further analyze the electronic structure of Fe atoms. The XANES curve of 0.4% Fe-CN displayed the absorption edge of 0.4% Fe-CN was located between the FeO and Fe₂O₃, indicating that the Fe atoms carried positive charges and the chemical valence was situated between + 2 and + 3 (Fig. 1e). Specifically, two small pre-edge peaks (A and B) at 7113.5 and 7117.5 eV were present, suggesting the presence of both Fe (II) and Fe (III) [20]. It is worth noting that the occurrence of peak C (~7131 eV) and D (~7138 eV). According to the reported works [21, 22], the relative intensity of the peak C and D is attributed to the distortion of the Fe-N₄ local structure. The primary shell peak located at 1.52 Å in FT-EXAFS spectra (Fig. 1f), which was different from Fe-Fe or Fe-O peak in Fe foil and Fe oxides. The peak at 1.52 Å in EXAFS fitting curve of 0.4% Fe-CN can be ascribed to Fe-N bond (Fig. 1g). The wavelet transform (WT) contour plots also displayed different distribution state from Fe foil and Fe oxides. In contrast to Fe foil, FeO and Fe₂O₃, no Fe-Fe or Fe-O bond was observed in 0.4% Fe-CN (Fig. S7), which excluded the presence of metal Fe nanoclusters. The average coordination number of Fe-N was 4 (Table S2), indicating that the formation of Fe-N₄ configuration in 0.4% Fe-CN (Fig. 1d). The above results confirmed the successful introduction of Fe single atoms with monatomic dispersion in CN support, which can be portrayed in Fig. 1g.

The surface chemical information of CN and 0.4% Fe-CN was analyzed using XPS (Fig. S8). The survey spectra revealed that C, N and O elements coexisted in the CN and 0.4% Fe-CN (Fig. S8a). Two peaks emerged at 710.9 and 724.4 eV were derived from Fe 2p_{3/2} and Fe 2p_{1/2}, respectively, while the peaks located at 716.9 and 732.4 eV were satellite peaks, indicating the formation of Fe-N bond in the CN matrix (Fig. 1h) [23]. In high-resolution C 1 s spectra (Fig. S8b), three peaks at 288.2, 286.3 and 284.8 eV corresponded to N-C≡N, C-N and C-C, respectively. In N 1 s XPS spectra, three peaks with binding energies of 401.2, 400.2 and 398.6 eV were assigned to sp³ tertiary N-H, N-(C)₃ groups and sp² C=N-C groups in the tri-s-triazine (pyridinic N), respectively (Fig. S8c) [24]. Moreover, in O 1 s XPS spectra (Fig. S8d), two peaks were observed, 531.9 eV for C-O bond and 532.8 eV for adsorbed H₂O [25]. In comparison of CN (73.5%), the content of pyridinic N increased to 74.6% in 0.4% Fe-CN, which was favorable to complex with Fe atoms (Table S3) [14]. The ⁵⁷Fe Mössbauer spectrum of 0.4% Fe-CN was shown in Fig. 1i and Table S4, which was least-squares fitted. The peaks fitted with three doublets (D1, D2 and D3) were ascribed to three structurally distinctive Fe-N₄ species. According to relevant literatures, the D1, D2 and D3 could be indexed to high-spin XY-Fe-N₄ site (X and Y represented weak axial ligand [26]), FeN₄ (similar to [FePC]²⁻ [27,28]) and low-spin FeN₄ site [29], respectively, which are all well-known active sites. The D1 (peak at 1.1 mm s⁻¹) and D2 (peak at 0.5 mm s⁻¹) were derived from Fe (II), and the D3 (peak at 0.3 mm s⁻¹) was assigned to Fe (III), which means the presence of Fe (III) and Fe (II) on the 0.4% Fe-CN. Further quantitative calculation revealed the ratios of Fe (III):Fe (II) was 38.3:61.7.

3.2. Photocatalytic performance of catalysts

The photocatalytic performance of Cr(VI) reduction over as-prepared samples was explored under visible light irradiation. Fig. S9 showed that the performance of the 0.4% Fe-CN-OA-vis system was considerably dependent on the OA dosage. The Cr(VI) removal time was shorter from

20 to 15 min when the OA dosage increased from 0.5 to 2.0 mM. However, when it continuously increased to 2.5 mM, the Cr(VI) reduction rate scarcely increased. Therefore, the optimal OA concentration was chosen as 2.0 mM in photocatalytic Cr(VI) reduction process. As shown in Fig. 2a, the Fe-CN catalysts displayed the enhanced performance for OA activation as compared to pristine CN. The introduced Fe single-atom sites in the CN support could facilitate the separation and transportation of the charge carriers, herein boosting the photocatalytic activity of Cr(VI) reduction. Apparently, the reduction followed the pseudo-first-order kinetics with the values of the rate constants (*k*) of 0.0273, 0.0746, 0.1394 and 0.0428 min⁻¹ over the CN, 0.2% Fe-CN, 0.4% Fe-CN and 0.6% Fe-CN catalysts with OA, respectively in Fig. S10. 0.4% Fe-CN catalysts revealed the fastest removal rate, which was 5.1 times than that of CN-OA-vis system. To investigate the influence of the surface area based on a quantitative comparison, we normalized the *k* value based on the surface area to fit Cr(VI) reduction process. While the normalized *k*_{surface} of 0.4% Fe-CN ($1.14 \times 10^{-3} \text{ g m}^{-2} \text{ min}^{-1}$) is still 2.43 times of CN ($4.69 \times 10^{-4} \text{ g m}^{-2} \text{ min}^{-1}$). These results suggested that there are other prior factors leading to the activity difference of the catalysts. Our previous work has indicated that OA alone displayed negligible Cr(VI) removal in the dark and under light irradiation [30]. The XPS spectrum of Cr 2p adsorbed on the 0.4% Fe-CN was shown in Fig. S11. The peaks at 577.2 and 586.8 eV corresponded to Cr (III), While the peaks at 579.9 and 589.3 eV were assigned to Cr(VI). These results indicated that Cr(VI) could be adsorbed on the catalyst surface. The adsorption was probably chemisorption [31]. In contrast to other systems, Cr(VI) reduction was significantly accelerated in the co-presence of visible light and OA, reaching 100% in 0.4% Fe-CN-OA-vis system within 15 min (Fig. 2b). Nearly 100% of Cr(VI) was removed within 20 min by 0.4% Fe-CN-OA-vis system in a wide pH range from 3.0 to 11.0 (Fig. 2c) and the solution pH values after the reaction maintained 2.5 ~ 3.0. The degradation rates were slightly decreased with the increase of pH values. Such a wide working pH demonstrated the great applicability of Fe-CN-OA-vis system, which was ascribed to the adjustment to acid condition in the Fe-CN-OA-vis system, resulting in excellent photocatalytic reduction performance [32]. The reusability of 0.4% Fe-CN powder catalyst was studied by cyclic removal of Cr(VI) under visible light irradiation (Fig. 2d). Over 97% of Cr(VI) was removed in all the three cycles by the powder catalysts, indicating the excellent reusability of 0.4% Fe-CN. The XRD patterns of recycled 0.4% Fe-CN catalyst displayed no obvious change in contrast to the fresh 0.4% Fe-CN, further demonstrating the structural stability of 0.4% Fe-CN catalyst in a reductive environment (Fig. 2e). The TEM image (Fig. S12) of 0.4% Fe-CN sample after reaction remained nanoflake shape without agglomeration phenomenon. The XPS spectrum of Cr 2p displayed two peaks located at 577.7 and 586.7 eV, which were assigned to Cr(III) 2p_{3/2} and Cr(III) 2p_{1/2}, respectively, indicating the Cr(VI) was successfully reduced into Cr(III) with less toxicity (Fig. 2f) [12].

We monitored the different operational factors during the Cr(VI) removal process. Fig. S13 showed the effects of Cr(VI) concentration and catalyst dosage in 0.4% Fe-CN-OA-vis system for Cr(VI) reduction, demonstrating the active sites on Fe-CN catalyst and species generated in system were vital for pollutant removal. As shown in Fig. 2g-h, the curves of 0.4% Fe-CN-OA-vis system in complex water matrix nearly overlapped with each other, suggesting excellent photocatalytic reduction performance except for CO₃²⁻. The inhibitory effect of CO₃²⁻ was expected due to the increase of solution pH and its function of radical scavenger in AOPs. The results above demonstrated excellent performance of the 0.4% Fe-CN-OA-vis system to adapt general circumstances of Cr(VI) wastewater. Then, we compared the reductive ability of the 0.4% Fe-CN catalyst with the recently reported catalysts in Cr(VI) reduction (Fig. 2i, the list of reference is shown in Table S5). Notably, the 0.4% Fe-CN displayed an extremely high reduction efficiency (100%) within the shortest time (15 min), which confirmed that engineering the CN incorporated single Fe atoms materials could offer promising catalysts for OA-assisted heavy metal reduction.

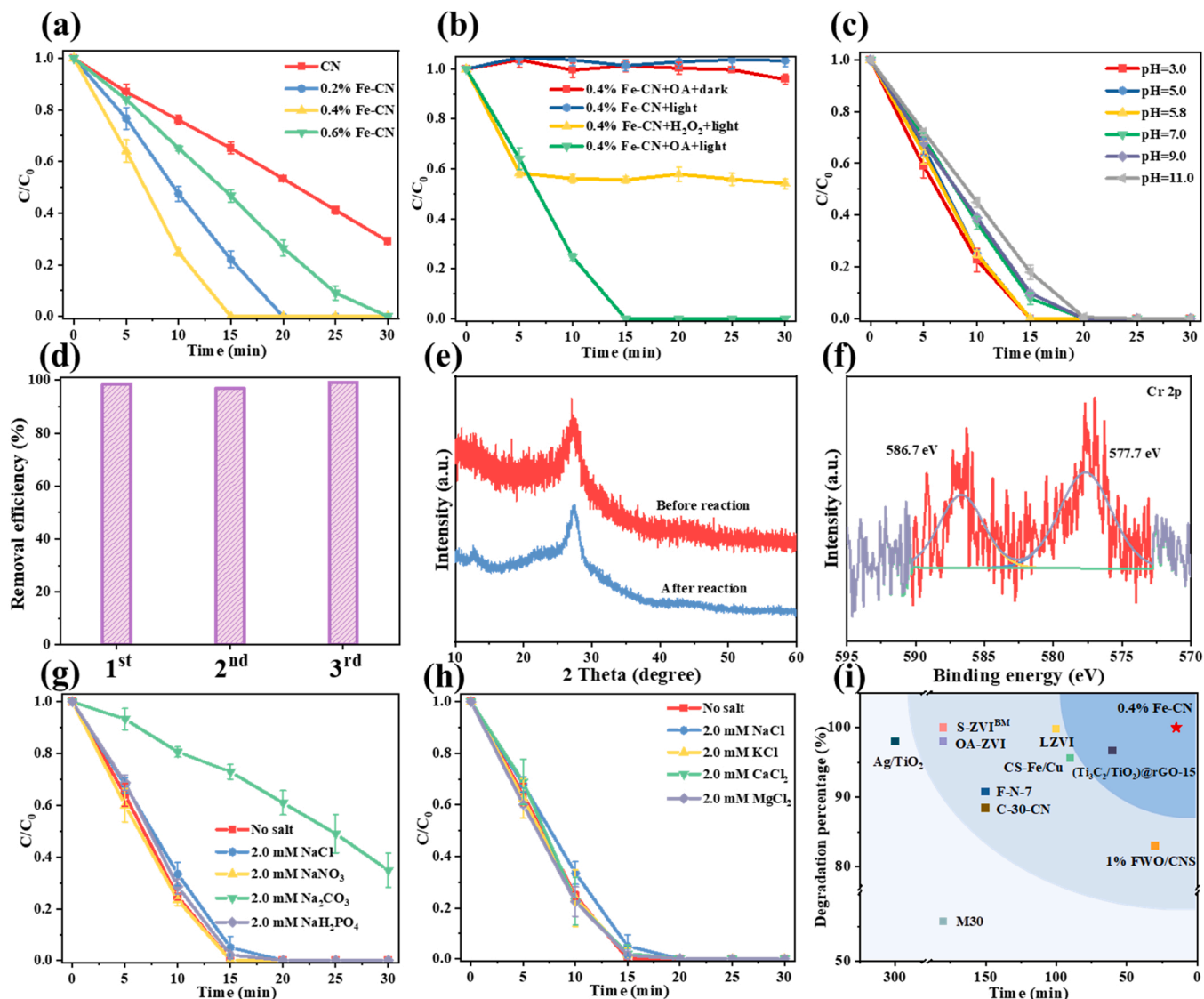


Fig. 2. Photocatalytic Cr(VI) reduction over (a) different catalysts, (b) different systems, and (c) different initial pH of solution. (d) The reusability of 0.4% Fe-CN. (e) XRD patterns of fresh and used 0.4% Fe-CN. (f) XPS spectrum of Cr 2p after the reaction. The effects of (g) inorganic anions and (h) cations in 0.4% Fe-CN-OA-vis system for Cr(VI) reduction. (i) Summary and comparison of Cr(VI) reduction performance for 0.4% Fe-CN and other catalysts.

Given the excellent catalytic performance of 0.4% Fe-CN-OA system, it was further applied to membrane treatment technology for Cr(VI)-containing wastewater in the continuous flow experiments in Fig. 3a-b. Membrane technology is more conducive to recovery and reuse of catalysts, which could promote the application in practical wastewater treatment [33]. 0.4% Fe-CN fibrous membranes were prepared by simple vacuum filtration. The light-yellow membrane ($d = 6.5$ cm) was sandwiched between a rubber ring and a small mesh support. The membrane morphology remained the same as origin after 10 h continuous treatment, which exhibited its great stability (Fig. 3c). SEM images of 0.4% Fe-CN fibrous membrane for surface and cross-sectional view showed the random stacking of 0.4% Fe-CN catalysts in Fig. 3d-e. Membrane flux and retention parameter were employed to investigate the performance of membrane materials. In Fig. 3f, the pristine fibrous membrane and 0.4% Fe-CN fibrous membrane showed water fluxes of 31.42 and $26.64 \text{ L m}^{-2} \text{ h}^{-1}$, respectively. These indicated that the presence of 0.4% Fe-CN catalysts prolonged the water retention time [34]. The retention time of Cr(VI) solution in catalytic layer was 8.1 s (Fig. S14) which was reckoned by Eq. 4. With the presence of OA, the removal of Cr(VI) by 0.4% Fe-CN fibrous membrane in photocatalysis experiment maintain 90% over 10 h (Fig. 3g), exhibiting the ultrahigh

activity and stability of 0.4% Fe-CN catalysts towards OA activation for Cr(VI) reduction.

3.3. Identification of reactive species

Radical trapping experiments were performed to identify the active species in the photocatalytic OA activation for Cr(VI) reduction (Fig. 4a-b). The process of Cr(VI) reduction was significantly inhibited when MVD was added, indicating $\bullet\text{CO}_2$ was the main active species in Cr(VI) reduction. The removal rate of Cr(VI) enhanced when AgNO_3 and IPA were added as trapping agents for e^- and $\bullet\text{OH}$, respectively. The electron traps resulted in more photogenerated holes, which contributed to the reaction of OA with h^+ . The trapping agents of $\bullet\text{OH}$, resulted in less oxidative radical species, which was benefit for reductive reaction of Cr(VI). Besides, the rate of reduction process was accelerated by excluding dissolved O_2 and conducting the experiment under a N_2 atmosphere. This result may be ascribed to the decrease of oxidative free radical species derived from dissolved O_2 . ESR spectra were performed to further analyze the active species in Fig. 4c-f. The characteristic peaks of $\text{DMPO}\bullet\text{CO}_2$ adduct, a sextet signal [35], were observed in CN-OA-vis and 0.4% Fe-CN-OA-vis systems, which derived from the OA

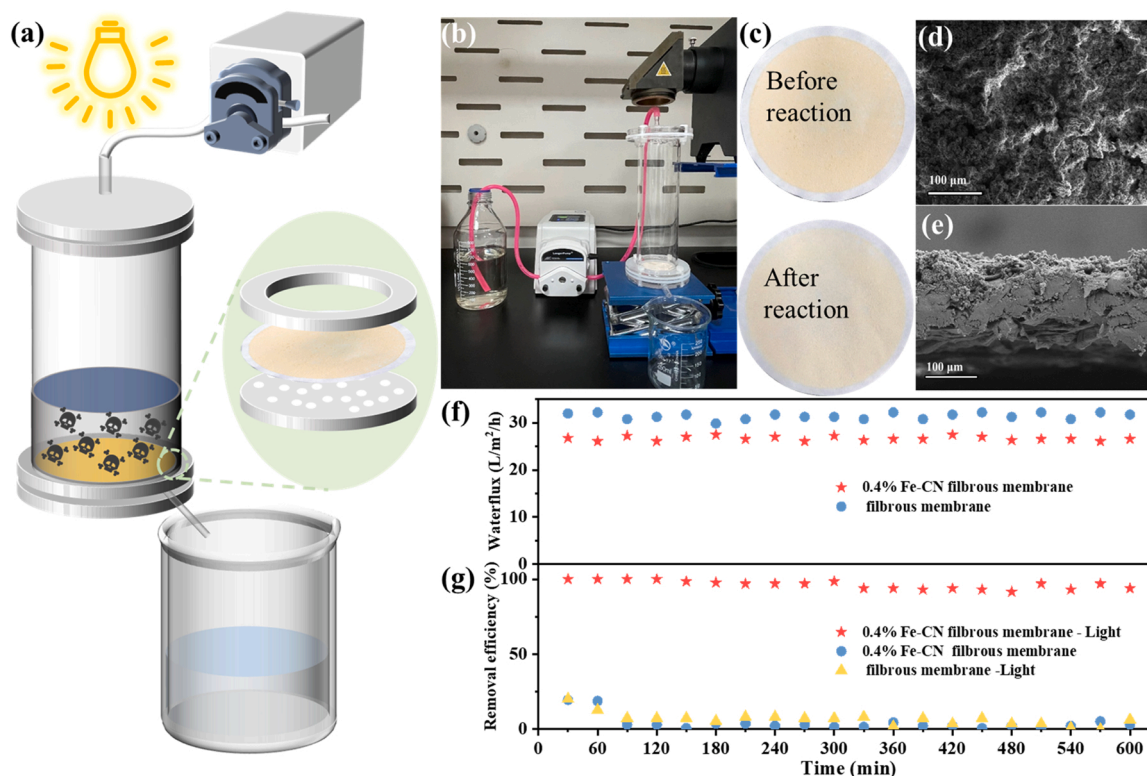


Fig. 3. (a) Schematic illustration of wastewater photo-treatment process. (b) Photograph of experiment device. (c) Photograph of 0.4% Fe-CN fibrous membrane before and after reaction. SEM images of the 0.4% Fe-CN fibrous membrane for (d) surface and (e) cross-sectional view. (f) The water performance of different membranes. (g) Cr(VI) reduction efficiency in different continuous flow systems.

activation in Fig. 4c. In addition, the DMPO- \bullet OH signal presented four-line relationship with relative intensity of 1:2:2:1 [36]. Significantly, \bullet CO₂ is the dominant active species, which account for the considerable promotion for Cr(VI) removal in the 0.4% Fe-CN-OA system. The absence of characteristic signal with the intensity ratio of 1:1:1:1 for DMPO- \bullet O₂ with or without OA (Fig. 4d) indicated that there was no \bullet O₂ involved in the reduction process. This result may be attributed to the weakened adsorption of 0.4% Fe-CN to O₂. The initial TEMPO- h^+ spectra with characteristic tri-peak intensity ratio of 1:1:1 with and without OA were shown in Fig. 4e. If TEMPO was oxidized by h^+ , triple peaks will get weaker, demonstrating the existence of photo-generated h^+ [37]. The signal of TEMPO- h^+ adduct had no change in the CN-OA-vis system under the visible irradiation. In contrast, the peaks remarkably weakened in 0.4% Fe-CN-OA-vis system, which means the introduction of Fe-N₄ sites can facilitate the separation and migration of photocarriers under the visible irradiation. The 0.4% Fe-CN-vis system showed no detectable change of TEMPO- h^+ signal without OA addition, which revealed that OA was required to generate h^+ under the visible irradiation in 0.4% Fe-CN-OA-vis system. In addition, 0.4% Fe-CN-OA-vis system displayed the TEMPO- h^+ signal intensity further decreased with the increase of irradiation time, suggesting the continuous generation of h^+ [25]. Meanwhile, the photogenerated h^+ reacted with OA to produce \bullet C₂O₄ additionally promotes the Cr(VI) reduction process [38]. The detected active species in different systems were concluded in Fig. 4f. The symbolic intensity from hollow to filled, implied that the introduction of Fe in CN enhanced the generation of h^+ , \bullet CO₂ and \bullet OH.

3.4. Mechanism discussion

There are two possible pathways about the mechanism of the OA activation by Fe-based catalysts. The first pathway was the ligand-to-metal charge transfer (LMCT) with the Fe(III) yielding Fe(II) and

oxidation products of oxalic ligand [39,40]. To better clear the Fe-CN-OA-vis activation mechanism, we quantified the different valence states of Fe in solution in Fig. 4g. Under visible light irradiation, the dissolved Fe(III) was detected maintain a stable level, while the dissolved Fe(II) could be barely detected even after the reaction was complete. Owing the conversion of Fe(II)/Fe(III) is requirement in the LMCT mechanism [41], this result was sufficient to rule out the possibility of LMCT mechanism in 0.4% Fe-CN-OA-vis system.

The other pathway of OA activation by Fe-based catalysts, photodissociation, involving the breakage of covalent bond, has been deeply explored in Fe-CN-OA-vis system. The interaction between OA and catalysts was explored via in-situ DRIFT spectra. CN-OA system (Fig. 5a) presented the peak at 1627 cm⁻¹ in the dark derived from OA and its deprotonated form [42], which decreased as light irradiation time increased due to the consumption of photo-induced holes (Fig. 5b). The similar characteristic peak was observed in 0.4% Fe-CN-OA system in the dark (Fig. 5c). Besides, the variation trend of peaks at 1627 cm⁻¹ in 0.4% Fe-CN-OA-vis system was the same as Fig. 5b. Nevertheless, a large number of new peaks emerged at 1717, 1416 and 1277 cm⁻¹ were attributed to the vibration of ν_s (C=O), ν_s (C-O) + ν (C-C) and ν_{as} (C-O), respectively. The peaks located at 1699 and 1683 cm⁻¹ were assigned as ν_{as} (C=O) [43] (Fig. 5d). Above results indicated the formation of inner-sphere complex between OA and Fe single atom, well matched with MB configuration [Fe^{III}(C₂O₄)]⁺, which further transferred to [Fe^{III}(C₂O₄)₃]³⁻ with highly photochemical activity, thus improving photocatalytic reduction performance [44]. According to the previous literature [45–47], the peaks were presumably ascribed to carboxylate, non-adsorbed C₂O₄²⁻ or its aqueous oxalic complexes.

Combined with the analysis of ligand and ROS, the possible ROS generation process in the Fe-CN-OA-vis system was proposed as follows. The first essential step of photocatalytic reaction was the adsorption of activator OA onto the catalyst surface. Under light irradiation, OA coordinated with Fe atoms to generate MB complex [Fe^{III}(C₂O₄)]⁺ on the

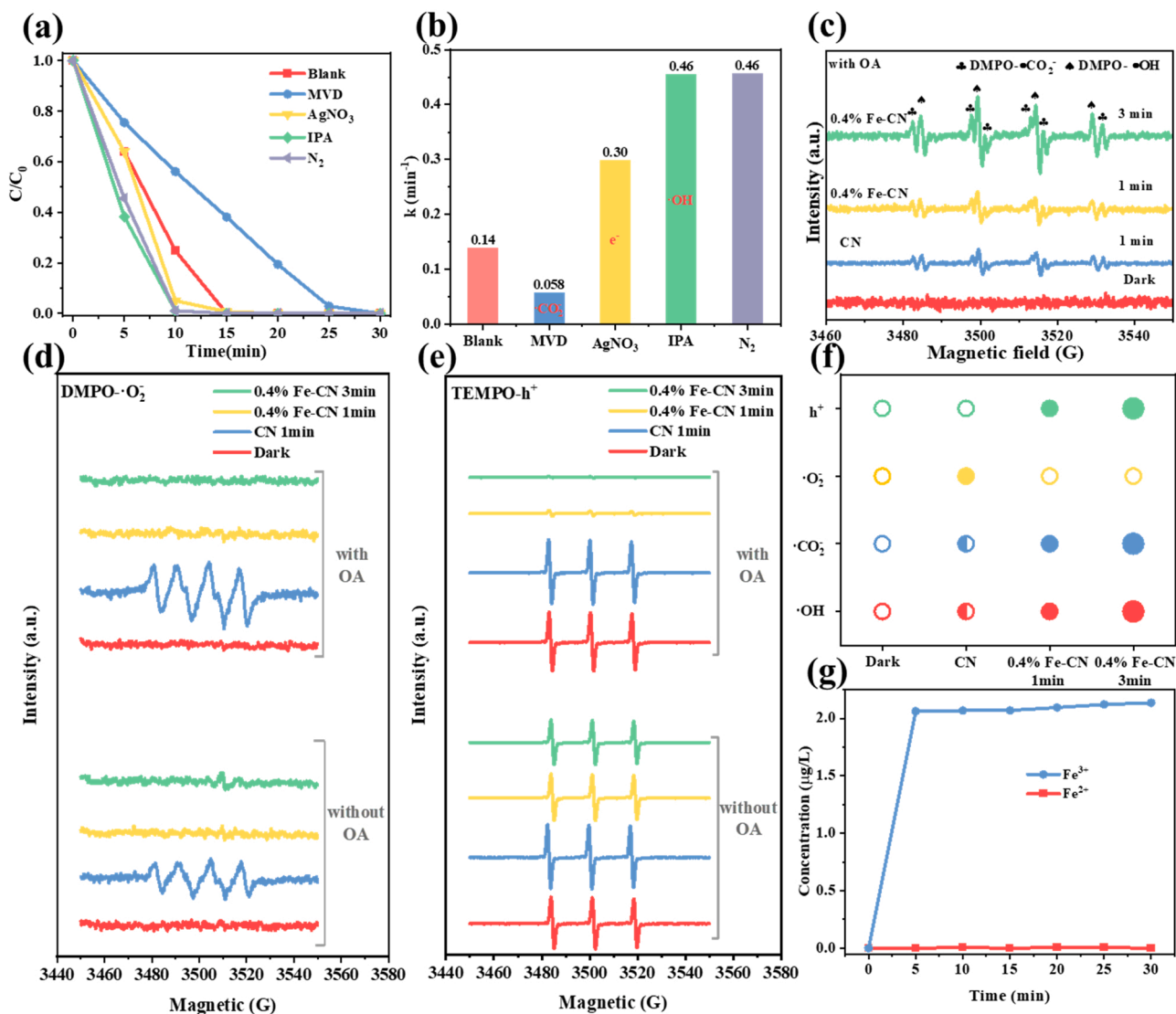
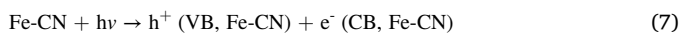
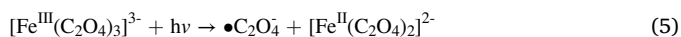


Fig. 4. (a) The radical trapping experiments for photocatalytic Cr(VI) reduction with (b) the corresponding reaction rate. ESR spectra of catalysts (c) with OA for DMPO-•CO₂⁻ and DMPO-•OH, with and without OA for (d) DMPO-•O₂⁻, (e) TEMPO-h⁺. (f) Qualitative and quantitative analysis of active species present in different OA activation systems. (g) Changes in the leached Fe concentration in 0.4% Fe-CN-OA-vis system.

surface. $[Fe^{III}(C_2O_4)_3]^{3-}$ further converted to high-activity compound $[Fe^{III}(C_2O_4)_3]^{3-}$, which produced $•C_2O_4$ and further produced $•CO_2$ via C-C cleaving (Eqs. 5–6, Fig. 5e) [48]. Meanwhile, photogenerated holes (Eq. 7) also reacted with OA to produce $•C_2O_4$ (Eq. 8). Subsequently, $•C_2O_4$ spontaneously decomposed to $•CO_2$ (Eq. 9). The resulting strong reductive radical $•CO_2$ was the main active species in photocatalytic Cr (VI) reduction (Eq. 10).



3.5. Optical and electrical properties of catalysts

Photoelectrochemical experiments were recorded to gain deeper insights into the photocatalytic reaction potential and photocarriers separation properties. As shown in DRS spectra (Fig. S15), CN exhibited strong absorption in visible-light region with the maximum absorption edge at 470 nm. The light absorption capacity showed an enhanced trend with the increase of Fe content. The band gap (E_g) of samples was estimated via the Kubelka-Munk equation: $\alpha h\nu = A(h\nu - E_g)^{n/2}$. The E_g of CN, 0.2% Fe-CN, 0.4% Fe-CN and 0.6% Fe-CN were calculated as 2.56, 2.47, 2.41 and 2.37 in Fig. S15, which decreased with the increase of Fe content. Subsequently, the conduction band (CB) potential was calculated by the results of Mott-Schottky measurements as shown in Fig. S16. Ultimately, the valence band (VB) potential could be determined by the equation: $E_{VB} = E_g + E_{CB}$. The obtained band structures of a series of samples were shown in Fig. S17. The improved separation efficiency of photogenerated carriers of 0.4% Fe-CN than CN was proved by photocurrent density spectra in Fig. S18a. Electrochemical impedance spectroscopy (EIS) depicted the 0.4% Fe-CN possessed smaller arc radius than that of CN in Fig. S18b, which was ascribed to the formation of Fe-N bond, thus promoting the transfer of photo-excited charges. Ultrafast

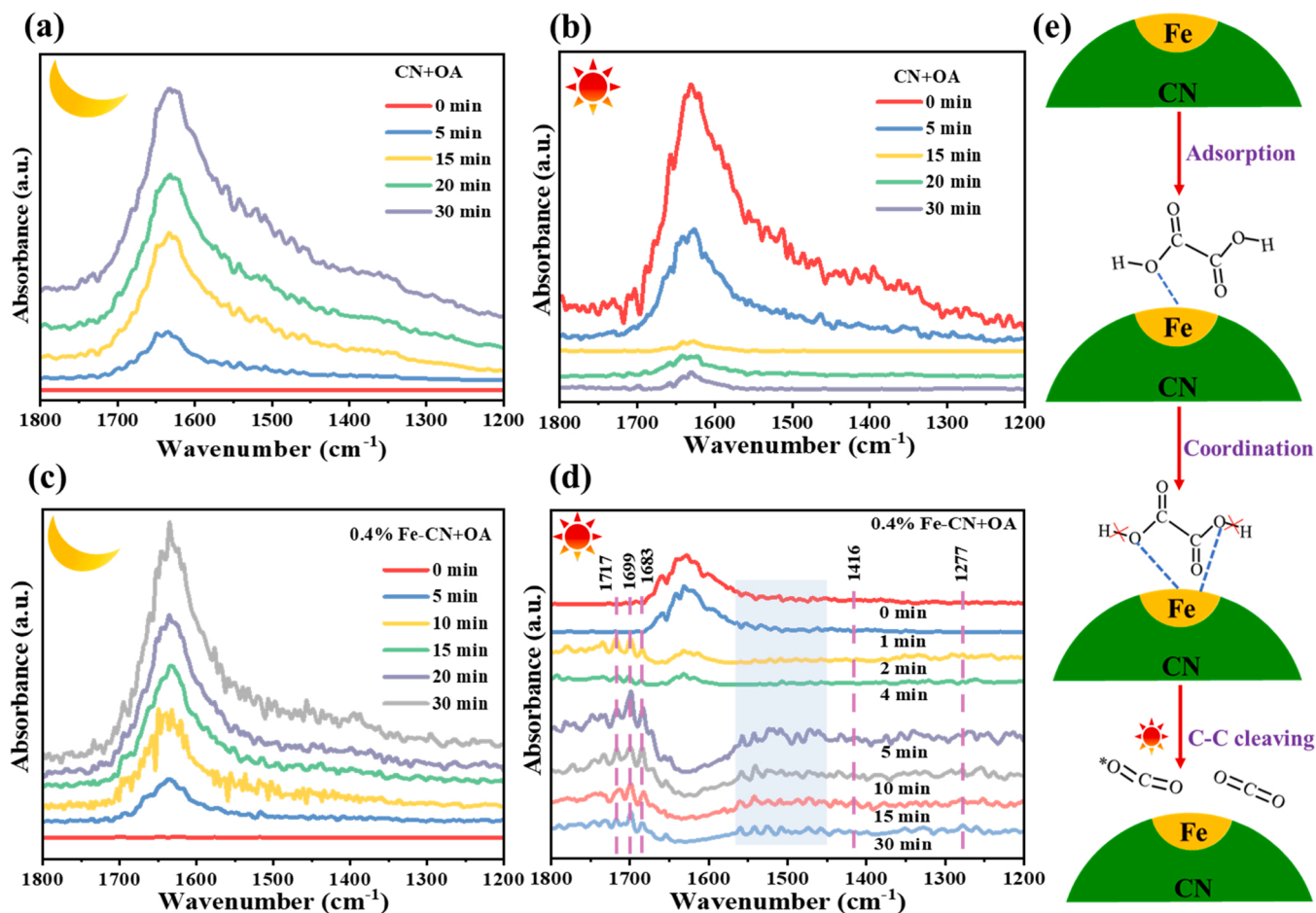


Fig. 5. In-situ DRIFT spectra of (a) CN-OA, (b) CN-OA-vis, (c) 0.4% Fe-CN-OA and (d) 0.4% Fe-CN-OA-vis system. (e) Proposed mechanism of $\bullet\text{CO}_2$ generation by OA coordination with Fe sites.

transient absorption spectroscopy (TAS) was performed to further shed light on the charge transfer dynamics. Fig. 6a-d displayed the TA color maps and differential absorbance spectra of CN and 0.4% Fe-CN. A wide band gap bleaching signal was emerged from 370 to 600 nm in CN, which was derived from the excitons trapped by CN defects. The negative absorption peak of 0.4% Fe-CN was ascribed to the ground-state bleaching [49]. Meanwhile, no positive absorption signal was observed in CN and 0.4% Fe-CN, indicating the exclusion of excited state absorption [50]. The corresponding kinetics of CN and 0.4% Fe-CN were shown in Fig. 6e-f, which were fitted with three exponential functions for CN ($\tau_1 = 1.72$ ps, $\tau_2 = 29.10$ ps, $\tau_3 = 1132.91$ ps) and 0.4% Fe-CN ($\tau_1 = 21.41$ ps, $\tau_2 = 1.32$ ps, $\tau_3 = 635.42$ ps). The prolonged component (τ_1) was assigned to electron transfer process to form excitons [49,51]. Then, the excitons relaxed and dissociated into free carriers (τ_2). The exciton decay to dissociated into free carriers in 0.4% Fe-CN was faster than that in CN [52], which further corroborated that the strong coordination interaction over Fe single atoms and N atoms could enhance the separation efficiency of carriers and thus promoted the reduction activity. Another shorter lifetime (τ_3) was ascribed to carrier recombination. Furthermore, dramatic PL quenching occurred after incorporation of Fe single atom contrast to CN, suggesting that intrinsic radiative recombination of photo-induced carriers in 0.4% Fe-CN was significantly inhibited (Fig. 6g) [53]. Meanwhile, the average lifetime of singlet excitons of the prepared catalysts decreased from 6.38 to 4.63 ns after incorporation of Fe single atoms, indicating the emergence of effective carrier separation and transfer pathway such as the non-radiative path formed by N-Fe-N interaction (Fig. 6h) [54]. Therefore, Fe single atom supported on CN could accept electrons and participate in

charge transfer, resulting in enhanced separation and migration of photocarriers just as shown in Fig. 6i. The above conclusions give a deep explain for the enhance of photocatalytic activation in 0.4% Fe-CN-OA-vis system than CN-OA-vis system to Cr(VI) reduction.

3.6. DFT calculations

DFT calculations were performed to analyze the mechanism of Cr(VI) reduction at atomic level. Fig. S19 presented the calculated band structure of CN and Fe-CN. The introduction of Fe single atom could narrow the E_g of CN, and the theoretical E_g of CN and Fe-CN were calculated as 1.20 and 1.15 eV, respectively. The density of states (DOS) shown in Fig. 7a-b implied that the valence band maximum was mainly contributed by N atoms. And the PDOS of N in Fe-CN was closer to the Fermi level than that of CN, indicating the electrons in Fe-CN were easier to be excited [53], which was in favor of separation and transfer of electrons. Fig. 7c-d displayed the electron density difference of OA adsorbed on CN and Fe-CN surfaces, respectively. When OA was coordinated with Fe atoms, the d-p conjugate between the d orbital of Fe atoms and p orbital of conjugated bond in OA could delocalize electrons, thus promoting coordination and increasing the electron cloud density [55]. The numbers of electrons transferred from CN and Fe-CN to OA were calculated to be 3.09 and 3.17, respectively. Moreover, the adsorption energies (E_{ads}) of OA adsorbed on the CN and Fe-CN were estimated to be -1.92 and -2.02 eV, respectively, implying that Fe-CN was likely to adsorb and activate OA. The Gibbs free energy of elementary activation step for OA on the surface of CN and Fe-CN, and the corresponding optimized structures of intermediates were shown in

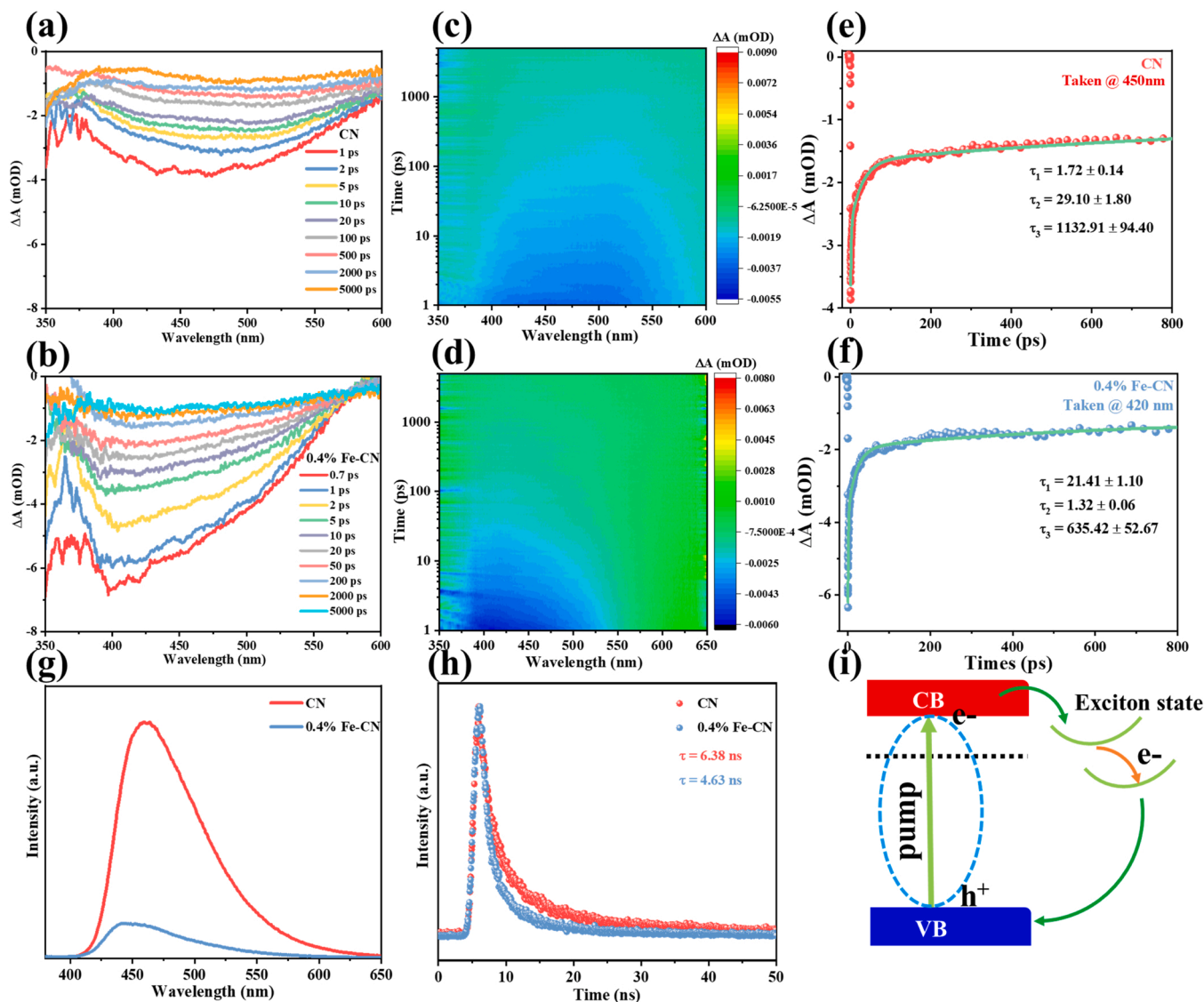


Fig. 6. Transient absorption spectra of (a) CN and (b) 0.4% Fe-CN with the corresponding (c-d) three-dimensional color maps and (e-f) TAS kinetics. (g) PL and (h) TRPL spectra of CN and 0.4% Fe-CN. (i) Schematic illustration of photocatalytic mechanism.

Fig. 7e. Initially, OA adsorbed and coordinated with the Fe atoms on the surface of catalysts to form $[\text{Fe}^{\text{III}}(\text{C}_2\text{O}_4)]^+$ complex, followed by conversion of $\bullet\text{C}_2\text{O}_4^-$ to $\bullet\text{CO}_2^-$ radical. Meanwhile, the OA also could be oxidized by photogenerated holes to generate little $\bullet\text{CO}_2^-$ radical. The Gibbs free energy of Fe-CN-OA system was significantly lower than that of CN-OA system, implying that Fe atoms promoted the OA activation, resulting in boost of Cr(VI) reduction performance.

4. Conclusion

In summary, the atomically dispersed Fe-CN catalyst was synthesized to activate OA for photocatalytic Cr(VI) reduction. The Fe-CN catalysts could facilitate photo-carriers separation and transfer via Fe-N interaction. Benefiting to the decreased Gibbs free energy of Fe-CN-OA system, the photocatalytic Cr(VI) reduction performance of Fe-CN obviously outperformed CN due to the generation of numerous reductive radical $\bullet\text{CO}_2^-$, which was mainly derived from $[\text{Fe}^{\text{III}}(\text{C}_2\text{O}_4)]^+$ complex formed by OA activation. Meanwhile, the introduction of Fe-N₄ sites promoted the generation of photogenerated h^+ and the reaction of h^+ with OA under the experiment condition. Under optimal conditions, the 0.4% Fe-CN-OA-vis system achieved 100% Cr(VI) reduction within 15 min.

Furthermore, 0.4% Fe-CN was applied to membrane separation technology which achieved high reductive activity (>90%) maintained a longtime (10 h). This work achieves efficient OA activation for photocatalytic Cr(VI) reduction and provides valuable insights into the development of OA activation in photocatalytic removal of heavy metal pollutants.

CRediT authorship contribution statement

J. Li: Project administration, Validation, Data curation, Resources, Investigation, Formal analysis, Writing – original draft. **X. Zhang:** Experiments, Software, Formal analysis, Writing – original draft. **J. Liu:** Experiments, Software, Formal analysis, Writing – original draft. **Z. Wang:** Experiments, Software, Formal analysis, Writing – original draft. **X. Zheng:** Experiments, Software, Formal analysis, Writing – original draft. **M. Zhang:** Data curation, Writing – review & editing, Supervision. **R. Chen:** Data curation, Writing – review & editing, Supervision. **Z. Liu:** Data curation, Writing – review & editing, Supervision.

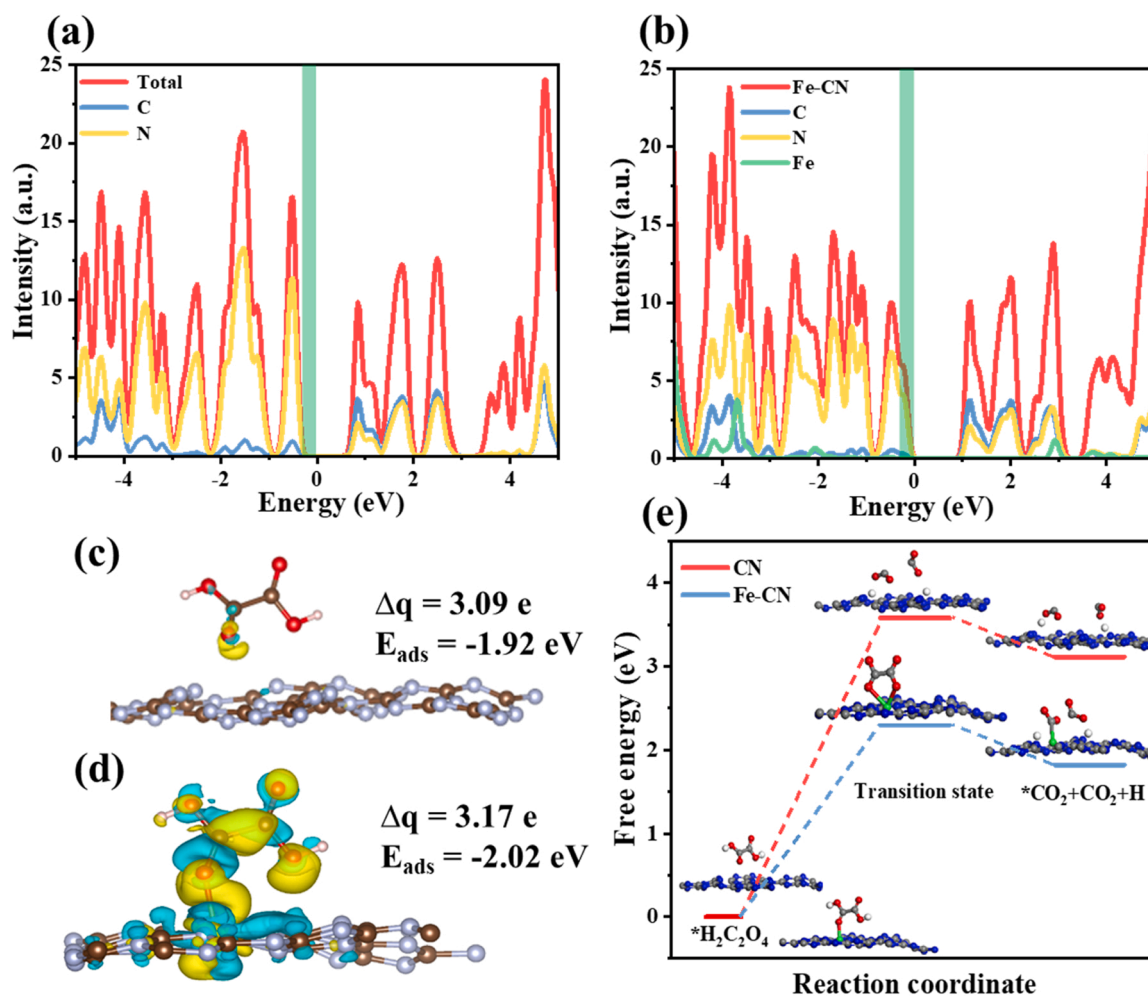


Fig. 7. Density of states of (a) CN and (b) Fe-CN. Electron density difference of OA adsorbed on (c) CN and (d) Fe-CN surfaces (the yellow and blue regions represent charge accumulation and depletion, respectively). (e) Gibbs free energy of OA activation on CN and Fe-CN.

Declaration of Competing Interest

The authors declare that they have no known competing financial interests or personal relationships that could have appeared to influence the work reported in this paper.

Data Availability

Data will be made available on request.

Acknowledgements

This work was financially supported by Outstanding Talent Research Fund and Young Talents Innovation Team Support Program of Zhengzhou University, China Postdoctoral Science Foundation (2020TQ0277, 2020M682328), Central Plains Science and Technology Innovation Leader Project (214200510006), Science and Technology Project of Henan Province (202102310274) and Postdoctoral Science Foundation of Henan province (202002010).

Appendix A. Supporting information

Supplementary data associated with this article can be found in the online version at doi:[10.1016/j.apcatb.2022.122068](https://doi.org/10.1016/j.apcatb.2022.122068).

References

- [1] P. Mytych, P. Cieřla, Z. Stasicka, Photoredox processes in the Cr(VI)–Cr(III)–oxalate system and their environmental relevance, *Appl. Catal. B: Environ.* 59 (2005) 161–170.
- [2] X. Su, A. Kushima, C. Halliday, J. Zhou, J. Li, T.A. Hatton, Electrochemically-mediated selective capture of heavy metal chromium and arsenic oxyanions from water, *Nat. Commun.* 9 (2018) 4701.
- [3] C. Zhao, L. Xue, H. Shi, W. Chen, Y. Zhong, Y. Zhang, Y. Zhou, K. Huang, Simultaneous degradation of p-nitrophenol and reduction of Cr(VI) in one step using microwave atmospheric pressure plasma, *Water Res.* 212 (2022), 118124.
- [4] S.K. Springthorpe, C.M. Dundas, B.K. Keitz, Microbial reduction of metal-organic frameworks enables synergistic chromium removal, *Nat. Commun.* 10 (2019) 5212.
- [5] M.A. Omole, V.A. Okello, V. Lee, L. Zhou, O.A. Sadik, C. Umbach, B. Sammakia, Catalytic reduction of hexavalent chromium using flexible nanostructured poly(amic acids), *ACS Catal.* 1 (2011) 139–146.
- [6] Y. Xiong, H. Li, C. Liu, L. Zheng, C. Liu, J.O. Wang, S. Liu, Y. Han, L. Gu, J. Qian, D. Wang, Single-atom Fe catalysts for Fenton-like reactions: roles of different N species, *Adv. Mater.* 34 (2022), e2110653.
- [7] Y. Guo, C. Li, Z. Gong, Y. Guo, X. Wang, B. Gao, W. Qin, G. Wang, Photocatalytic decontamination of tetracycline and Cr(VI) by a novel α -FeOOH/FeS₂ photocatalyst: one-pot hydrothermal synthesis and Z-scheme reaction mechanism insight, *J. Hazard. Mater.* 397 (2020), 122580.
- [8] H. Zhang, C. Li, L. Lyu, C. Hu, Surface oxygen vacancy inducing peroxymonosulfate activation through electron donation of pollutants over cobalt-zinc ferrite for water purification, *Appl. Catal. B: Environ.* 270 (2020), 118874.
- [9] S. Bassaid, D. Robert, M. Chaib, Use of oxalate sacrificial compounds to improve the photocatalytic performance of titanium dioxide, *Appl. Catal. B: Environ.* 86 (2009) 93–97.
- [10] Y. Pan, Q. Wang, M. Zhou, J. Cai, Y. Tian, Y. Zhang, Kinetic and mechanism study of UV/pre-magnetized-Fe(0)/oxalate for removing sulfamethazine, *J. Hazard. Mater.* 398 (2020), 122931.

- [11] M. Huang, T. Zhou, X. Wu, J. Mao, Distinguishing homogeneous-heterogeneous degradation of norfloxacin in a photochemical Fenton-like system ($\text{Fe}_3\text{O}_4/\text{UV}/\text{oxalate}$) and the interfacial reaction mechanism, *Water Res.* 119 (2017) 47–56.
- [12] J. Li, C. Xiao, K. Wang, Y. Li, G. Zhang, Enhanced generation of reactive oxygen species under visible light irradiation by adjusting the exposed facet of FeWO_4 nanosheets to activate oxalic acid for organic pollutant removal and Cr(VI) reduction, *Environ. Sci. Technol.* 53 (2019) 11023–11030.
- [13] X. Zhao, X. Li, Z. Zhu, W. Hu, H. Zhang, J. Xu, X. Hu, Y. Zhou, M. Xu, H. Zhang, G. Hu, Single-atom Co embedded in BCN matrix to achieve 100% conversion of peroxymonosulfate into singlet oxygen, *Appl. Catal. B: Environ.* 300 (2022), 120759.
- [14] H. Cao, J. Wang, J.-H. Kim, Z. Guo, J. Xiao, J. Yang, J. Chang, Y. Shi, Y. Xie, Different roles of Fe atoms and nanoparticles on g- C_3N_4 in regulating the reductive activation of ozone under visible light, *Appl. Catal. B: Environ.* 296 (2021), 120362.
- [15] P. Duan, J. Pan, W. Du, Q. Yue, B. Gao, X. Xu, Activation of peroxymonosulfate via mediated electron transfer mechanism on single-atom Fe catalyst for effective organic pollutants removal, *Appl. Catal. B: Environ.* 299 (2021), 120714.
- [16] L. Zhang, X. Jiang, Z. Zhong, L. Tian, Q. Sun, Y. Cui, X. Lu, J. Zou, S. Luo, Carbon nitride supported high-loading Fe single-atom catalyst for activation of peroxymonosulfate to generate $^1\text{O}_2$ with 100% selectivity, *Angew. Chem. Int. Ed.* 60 (2021) 21751–21755.
- [17] Y. Ju, H. Li, Z. Wang, H. Liu, S. Huo, S. Jiang, S. Duan, Y. Yao, X. Lu, F. Chen, Solar-driven on-site H_2O_2 generation and tandem photo-Fenton reaction on a triphase interface for rapid organic pollutant degradation, *Chem. Eng. J.* 430 (2022), 133168.
- [18] X. Ma, Z. Zhang, C. Yu, Q. Fan, L. Wei, A novel nitrogen-deficient g- C_3N_4 photocatalyst fabricated via liquid phase reduction route and its high photocatalytic performance for hydrogen production and Cr(VI) reduction, *Mater. Res. Bull.* 129 (2020), 110909.
- [19] C. Song, Q. Zhan, F. Liu, C. Wang, H. Li, X. Wang, X. Guo, Y. Cheng, W. Sun, L. Wang, J. Qian, B. Pan, Overturned loading of inert CeO_2 to active Co_3O_4 for unusually improved catalytic activity in Fenton-like reactions, *Angew. Chem. Int. Ed.* (2022) e202200406.
- [20] S. An, G. Zhang, T. Wang, W. Zhang, K. Li, C. Song, J.T. Miller, S. Miao, J. Wang, X. Guo, High-density ultra-small clusters and single-atom Fe sites embedded in graphitic carbon nitride (g- C_3N_4) for highly efficient catalytic advanced oxidation processes, *ACS Nano* 12 (2018) 9441–9450.
- [21] Y.J. Sa, D.J. Seo, J. Woo, J.T. Lim, J.Y. Cheon, S.Y. Yang, J.M. Lee, D. Kang, T. J. Shin, H.S. Shin, H.Y. Jeong, C.S. Kim, M.G. Kim, T.Y. Kim, S.H. Joo, A general approach to preferential formation of active Fe-N₃ sites in Fe-N/C electrocatalysts for efficient oxygen reduction reaction, *J. Am. Chem. Soc.* 138 (2016) 15046–15056.
- [22] Q. Jia, N. Ramaswamy, H. Hafiz, U. Tylus, K. Strickland, G. Wu, B. Barbiellini, A. Bansil, E.F. Holby, P. Zelenay, S. Mukerjee, Experimental observation of redox-induced Fe-N switching behavior as a determinant role for oxygen reduction activity, *ACS Nano* 9 (2015) 12496–12505.
- [23] X. Zhao, X. Li, Z. Bi, Y. Wang, H. Zhang, X. Zhou, Q. Wang, Y. Zhou, H. Wang, G. Hu, Boron modulating electronic structure of FeN_4C to initiate high-efficiency oxygen reduction reaction and high-performance zinc-air battery, *J. Energy Chem.* 66 (2022) 514–524.
- [24] F. Chen, X.L. Wu, C. Shi, H. Lin, J. Chen, Y. Shi, S. Wang, X. Duan, Molecular engineering toward pyrrolic N-rich M-N₄ (M = Cr, Mn, Fe, Co, Cu) single-atom sites for enhanced heterogeneous Fenton-like reaction, *Adv. Funct. Mater.* 31 (2021) 2007877.
- [25] J. Ma, Y. Li, D. Jin, X. Yang, G. Jiao, K. Liu, S. Sun, J. Zhou, R. Sun, Reasonable regulation of carbon/nitride ratio in carbon nitride for efficient photocatalytic reforming of biomass-derived feedstocks to lactic acid, *Appl. Catal. B: Environ.* 299 (2021), 120698.
- [26] N.R. Sahaie, U.I. Kramm, J. Steinberg, Y. Zhang, A. Thomas, T. Reier, J. P. Paraknowitsch, P. Strasser, Quantifying the density and utilization of active sites in non-precious metal oxygen electroreduction catalysts, *Nat. Commun.* 6 (2015) 8618.
- [27] M. Kübler, S. Wagner, T. Jurzinsky, S. Paul, N. Weidler, E.D. Gomez Villa, C. Cremers, U.I. Kramm, Impact of surface functionalization on the intrinsic properties of the resulting Fe-N-C catalysts for fuel cell applications, *Energy Technol.* 8 (2020) 2000433.
- [28] U.I. Kramm, I. Abs-Wurmbach, I. Herrmann-Geppert, J. Radnik, S. Fiechter, P. Bogdanoff, Influence of the electron-density of FeN_4 -centers towards the catalytic activity of pyrolyzed FeTMPPCL-based ORR-electrocatalysts, *J. Electrochem. Soc.* 158 (2011) B69–B78.
- [29] U.I. Kramm, I. Herrmann-Geppert, J. Behrends, K. Lips, S. Fiechter, P. Bogdanoff, On an easy way to prepare metal-nitrogen doped carbon with exclusive presence of MeN_4 -type sites active for the ORR, *J. Am. Chem. Soc.* 138 (2016) 635–640.
- [30] J. Liu, Q. Liu, J. Li, X. Zheng, Z. Liu, X. Guan, Photochemical conversion of oxalic acid on heterojunction engineered $\text{FeWO}_4/\text{g-C}_3\text{N}_4$ photocatalyst for high-efficient synchronous removal of organic and heavy metal pollutants, *J. Clean. Prod.* 363 (2022), 132527.
- [31] H. Zou, E. Hu, S. Yang, L. Gong, F. He, Chromium(VI) removal by mechanochemically sulfidated zero valent iron and its effect on dechlorination of trichloroethene as a co-contaminant, *Sci. Total Environ.* 650 (2019) 419–426.
- [32] Q. Yan, C. Lian, K. Huang, L. Liang, H. Yu, P. Yin, J. Zhang, M. Xing, Constructing an acidic microenvironment by MoS_2 in heterogeneous Fenton reaction for pollutant control, *Angew. Chem. Int. Ed.* 60 (2021) 17155–17163.
- [33] Z. Wang, E. Almatrafi, H. Wang, H. Qin, W. Wang, L. Du, S. Chen, G. Zeng, P. Xu, Cobalt single atoms anchored on oxygen-doped tubular carbon nitride for efficient peroxymonosulfate activation: Simultaneous coordination structure and morphology modulation, *Angew. Chem. Int. Ed.* 61 (2022), e202202338.
- [34] Z. Lu, G. Zhou, B. Li, Y. Xu, P. Wang, H. Yan, M. Song, C. Ma, S. Han, X. Liu, Heterotopic reaction strategy for enhancing selective reduction and synergistic oxidation ability through trapping Cr(VI) into specific reaction site: a stable and self-cleaning ion imprinted CdS/HTNW photocatalytic membrane, *Appl. Catal. B: Environ.* 301 (2022).
- [35] N. Chen, Y. Wan, G. Zhan, X. Wang, M. Li, L. Zhang, Simulated solar light driven roxarsone degradation and arsenic immobilization with hematite and oxalate, *Chem. Eng. J.* 384 (2020), 123254.
- [36] S. Guo, H. Wang, W. Yang, H. Fida, L. You, K. Zhou, Scalable synthesis of Ca-doped $\alpha\text{-Fe}_2\text{O}_3$ with abundant oxygen vacancies for enhanced degradation of organic pollutants through peroxymonosulfate activation, *Appl. Catal. B: Environ.* 262 (2020), 118250.
- [37] X. Li, Y. Qiu, Z. Zhu, H. Zhang, D. Yin, Novel recyclable Z-scheme g- C_3N_4 /carbon nanotubes/ $\text{Bi}_{25}\text{FeO}_{40}$ heterostructure with enhanced visible-light photocatalytic performance towards tetracycline degradation, *Chem. Eng. J.* 429 (2022), 132130.
- [38] D. Lei, J. Xue, X. Peng, S. Li, Q. Bi, C. Tang, L. Zhang, Oxalate enhanced synergistic removal of chromium(VI) and arsenic(III) over $\text{ZnFe}_2\text{O}_4/\text{g-C}_3\text{N}_4$: Z-scheme charge transfer pathway and photo-Fenton like reaction, *Appl. Catal. B: Environ.* 282 (2021), 119578.
- [39] I. Kretschmer, A.M. Senn, J.M. Meichtry, G. Custo, E.B. Halac, R. Dillert, D. W. Bahnemann, M.I. Litter, Photocatalytic reduction of Cr(VI) on hematite nanoparticles in the presence of oxalate and citrate, *Appl. Catal. B: Environ.* 242 (2019) 218–226.
- [40] Q. Lan, H. Liu, F.-B. Li, F. Zeng, C.-S. Liu, Effect of pH on pentachlorophenol degradation in irradiated iron/oxalate systems, *Chem. Eng. J.* 168 (2011) 1209–1216.
- [41] T. Xu, R. Zhu, H. Shang, Y. Xia, X. Liu, L. Zhang, Photochemical behavior of ferrihydrite-oxalate system: interfacial reaction mechanism and charge transfer process, *Water Res.* 159 (2019) 10–19.
- [42] P. Persson, K. Axe, Adsorption of oxalate and malonate at the water-goethite interface: molecular surface speciation from IR spectroscopy, *Geochim. Cosmochim. Acta* 69 (2005) 541–552.
- [43] S.C. Borowski, J. Biswakarma, K. Kang, W.D.C. Schenkeveld, J.G. Hering, J. D. Kubicki, S.M. Kraemer, S.J. Hug, Structure and reactivity of oxalate surface complexes on lepidocrocite derived from infrared spectroscopy, DFT-calculations, adsorption, dissolution and photochemical experiments, *Geochim. Cosmochim. Acta* 226 (2018) 244–262.
- [44] T. Xu, Y. Fang, T. Tong, Y. Xia, X. Liu, L. Zhang, Environmental photochemistry in hematite-oxalate system: Fe(III) -oxalate complex photolysis and ROS generation, *Appl. Catal. B: Environ.* 283 (2021), 119645.
- [45] B.J. Stephen, H.Y. Tae, J.S. Aaron, J. Gordon, E. Brown, Adsorption of organic matter at mineral/water interfaces: 3. implications of surface dissolution for adsorption of oxalate, *Langmuir* 20 (2004) 11480–11492.
- [46] K. Axe, P. Persson, Time-dependent surface speciation of oxalate at the water-boehmite (a- AlOOH) interface: implications for dissolution, *Geochim. Cosmochim. Acta* 65 (2001) 4481–4492.
- [47] E.D. Flynn, J.G. Catalano, Competitive and cooperative effects during nickel adsorption to iron oxides in the presence of oxalate, *Environ. Sci. Technol.* 51 (2017) 9792–9799.
- [48] C. Kang, H. Rao, Y. Fang, J. Zeng, Z. Pan, X. Zhong, Antioxidative stannous oxalate derived lead-free stable CsSnX_3 ($\text{X}=\text{Cl}, \text{Br}, \text{I}$) perovskite nanocrystals, *Angew. Chem. Int. Ed.* 60 (2021) 660–665.
- [49] F. Li, X. Yue, D. Zhang, J. Fan, Q. Xiang, Targeted regulation of exciton dissociation in graphitic carbon nitride by vacancy modification for efficient photocatalytic CO_2 reduction, *Appl. Catal. B: Environ.* 292 (2021), 120179.
- [50] H. Liu, P. Tan, Y. Liu, H. Zhai, W. Du, X. Liu, J. Pan, Ultrafast interfacial charge evolution of the Type-II cadmium Sulfide/Molybdenum disulfide heterostructure for photocatalytic hydrogen production, *J. Colloid Interface Sci.* 619 (2022) 246–256.
- [51] Y. Shi, Q. Zhao, J. Li, G. Gao, J. Zhi, Onion-like carbon-embedded graphitic carbon nitride for enhanced photocatalytic hydrogen evolution and dye degradation, *Appl. Catal. B: Environ.* 308 (2022), 121216.
- [52] H. Wang, D. Yong, S. Chen, S. Jiang, X. Zhang, W. Shao, Q. Zhang, W. Yan, B. Pan, Y. Xie, Oxygen-vacancy-mediated exciton dissociation in BiOBr for boosting charge-carrier-involved molecular oxygen activation, *J. Am. Chem. Soc.* 140 (2018) 1760–1766.
- [53] L. Zeng, J.-W. Chen, L. Zhong, W. Zhen, Y.Y. Tay, S. Li, Y.-G. Wang, L. Huang, C. Xue, Synergistic effect of Ru-N_4 sites and Cu-N_3 sites in carbon nitride for highly selective photocatalytic reduction of CO_2 to methane, *Appl. Catal. B: Environ.* 307 (2022), 121154.
- [54] G. Zhao, W. Li, H. Zhang, W. Wang, Y. Ren, Single atom Fe-dispersed graphitic carbon nitride (g- C_3N_4) as a highly efficient peroxymonosulfate photocatalytic activator for sulfamethoxazole degradation, *Chem. Eng. J.* 430 (2022), 132937.
- [55] M. Liao, X. Wang, S. Cao, M. Li, X. Peng, L. Zhang, Oxalate modification dramatically promoted Cr(VI) removal with zero-valent iron, *ACS ES&T Water* 1 (2021) 2109–2118.